

## Article

# Al<sub>2</sub>O<sub>3</sub> Thin Layer Formed inside Porous Membrane Using Spray Synthesis Method and Its Application

Masato Imai <sup>1,\*</sup>, Tadahiko Kubota <sup>2</sup>, Atsushi Miyazawa <sup>3</sup>, Masahiro Aoki <sup>4</sup>, Haruna Mori <sup>4</sup>, Yuta Komaki <sup>5</sup> and Kenji Yoshino <sup>1,\*</sup>

<sup>1</sup> The Electrical and Electronic Engineering Program, Faculty of Engineering, University of Miyazaki, 1-1 Gakuen Kibanadai-nishi, Miyazaki 889-2192, Japan

<sup>2</sup> Yokohama Battery Science Corporation, 3-21-11 Nakazawa, Asahi, Yokohama 241-0814, Japan

<sup>3</sup> Tosoh Corporation, 2743-1, Hayakawa, Ayase 252-1123, Japan

<sup>4</sup> Tosoh Finechem Corporation, 4555 Kaisei, Shunan 746-0006, Japan

<sup>5</sup> Engineering Post Graduate Course Engineering Specialty, Faculty of Engineering, University of Miyazaki, 1-1 Gakuen Kibanadai-nishi, Miyazaki 889-2192, Japan

\* Correspondence: m\_imai@cc.miyazaki-u.a.jp (M.I.); t0b114u@cc.miyazaki-u.ac.jp (K.Y.)

**Abstract:** Aluminum oxide (Al<sub>2</sub>O<sub>3</sub>) films have been investigated for use in various applications, and numerous deposition techniques have been reported. The spray synthesis method has the advantage of forming a thin layer of crystal at low temperatures using the appropriate precursors. A precursor prepared by diluting Methylaluminoxane with N-methyl pyrrolidone was sprayed onto a porous membrane while varying conditions such as the substrate temperature, feeding speed, and spray amount. The solution penetrated the film during spray application, and the ultra-thin layers deposited on the side wall of the internal pores were observed using a cross-sectional transmission electron microscope (XTEM). The lattice image obtained using the TEM and the composition analysis conducted using a scanning TEM and an energy-dispersive X-ray spectroscopy suggest that this thin layer is a layer of Al<sub>2</sub>O<sub>3</sub>. The formation of Al<sub>2</sub>O<sub>3</sub> occurred at lower temperatures than in previous reports. This is a major advantage for applications with low-melting-point materials. The most suitable spraying conditions were determined based on the state of deposition on the surface and inside the membrane. These conditions were applied to a three-layer separator for lithium-ion batteries and their effect on thermal stability was investigated. Through heating experiments and XRD analysis, it was confirmed that the shrinkage and melting of the separator are suppressed by spraying. This process can be expected to have wide applications in low-melting-point materials such as polyolefin.

**Keywords:** aluminum oxide; spray synthesis method; methylaluminoxane; porous membrane; lithium-ion battery



**Citation:** Imai, M.; Kubota, T.; Miyazawa, A.; Aoki, M.; Mori, H.; Komaki, Y.; Yoshino, K. Al<sub>2</sub>O<sub>3</sub> Thin Layer Formed inside Porous Membrane Using Spray Synthesis Method and Its Application. *Crystals* **2024**, *14*, 195. <https://doi.org/10.3390/cryst14020195>

Academic Editor: Vladislav V. Kharton

Received: 30 December 2023

Revised: 12 February 2024

Accepted: 15 February 2024

Published: 17 February 2024



**Copyright:** © 2024 by the authors. Licensee MDPI, Basel, Switzerland. This article is an open access article distributed under the terms and conditions of the Creative Commons Attribution (CC BY) license (<https://creativecommons.org/licenses/by/4.0/>).

## 1. Introduction

Aluminum oxide (Al<sub>2</sub>O<sub>3</sub>) films have been investigated for use in various applications, such as in semiconductor devices, organic light-emitting diodes, solar cells, lithium-ion batteries (LIBs), solid oxide fuel cells (SOFCs), and nuclear technology [1–8]. Numerous deposition techniques have been used to fabricate Al<sub>2</sub>O<sub>3</sub> thin layers for each application, such as atomic layer deposition (ALD) [9], pulsed laser deposition (PLD) [10], magnetron sputtering [11], the sol–gel method [12], and spray synthesis [13,14].

ALD is a chemical self-limited deposition technique that uses two chemical precursors in most cases. The substrate is placed at a given temperature and pressure so that the material can be deposited layer by layer on the surface of the substrate in the chamber. ALD is a key process in fabricating semiconductor devices and is one of the tools used for synthesizing nanomaterials. PLD is a physical vapor deposition technique where a high-power pulsed laser beam is focused inside a vacuum chamber to strike the target of the

material that is to be deposited. This material is vaporized from the target, which deposits it as a thin film on a substrate in an ultra-high vacuum. The application of this technique spans the fields of optical devices, electronic materials, sensors and actuators, biomaterials, and organic polymers. Magnetron sputtering is a technique in which the target material is bombarded with high-energy ions to eject atoms from the target, which then deposit onto a substrate to form a thin film. This technique is widely used in the semiconductor industry. The sol-gel method produces solid materials from small molecules. The process involves the conversion of monomers into a sol, which acts as the precursor for a gel of either discrete particles or network polymers. The sol-gel process is used to produce ceramic nanoparticles.

The spray synthesis technique consists of three main stages: the composition of the precursor solution, aerosol generation and transport, and the synthesis process. Each of these steps is tailored to the final chemical and physical properties of the target material, and the materials and processes selected at each stage affect the subsequent stages [15,16]. The solvent in the precursor solution is selected by considering the solubility of the precursor compound and its physical properties such as density, evaporation rate, and viscosity. The physical properties of the final material formed, such as morphology and crystallinity, are established by the aerosol droplet size distribution. The average droplet diameter is estimated by the liquid surface tension, the mass flow rate of liquid and gas, the density of gas, the diameter of the spraying solution inlet orifice, and gas velocity according to the aerosol formation mechanism [17]. The material synthesis process is determined by several parameters such as substrate temperature, droplet size, and their flow speed at the reactive zone [15].

The spray synthesis technique has an industrial advantage because it is a low-cost process that does not require vacuum equipment, and the material can be formed over a wide area. There are many reports of films being deposited on various substrates using this method [18–21]. It is also reported that thin layers of crystals can be formed at low temperatures by using appropriate precursors such as diethylzinc-based solution and Methylaluminoxane solution [22–24]. This advantage leads to potential applications for low-melting-point materials such as polyolefins.

LIBs with high power density and excellent cycle life are increasingly used for electronic vehicles, power tools, and portable electronic devices in the power-source market, but urgently require a higher energy density [25–28]. As energy density increases, improving the safety of LIBs has become an urgent issue [29,30]. The separator in an LIB, which maintains the physical isolation between electrodes, as well as an electrolyte container to provide Li<sup>+</sup> ion transport channels during cycling, is a critical part for improving battery performance such as cycle life, energy density, power density, and safety [31–33]. Many proposals have been made to improve thermal stability, coating various inorganic particles on the separator surface using a simple bar process or a dip process [34–37].

In this study, a porous membrane was sprayed using a previously reported precursor [24], and the effects of the spray conditions on the deposition state, such as substrate temperature, feeding speed, and spray amount, were investigated. Thin layers were observed as sprayed inside the membrane, suggesting a layer of Al<sub>2</sub>O<sub>3</sub>. Then, we investigated the effects of spray application on resistance and thermal stability using a commercially available three-layer separator. After spray application, the separator did not show increased resistance, and shrinkage and melting were suppressed, resulting in an improvement in thermal stability.

## 2. Materials and Methods

The precursor prepared by diluting Methylaluminoxane (MAO) with N-methylpyrrolidone (NMP) to an Al concentration of 1 wt% was used for spray application. MAO is a mixture of organoaluminium compounds expressed by the approximate formula (Al(CH<sub>3</sub>)O)<sub>n</sub> [38]. NMP is frequently used in LIB manufacturing as a solvent for cleaning electrodes [39].

Two types of porous membranes were used as substrates for spray application. A monolayer membrane (Celgard 2400, thickness = 25  $\mu\text{m}$ ) composed of a polypropylene (PP) matrix with pores was used to investigate the relationship between the spray conditions and the deposition state on the surface and inside. The effects of spray application on resistance and thermal stability were investigated using a three-layer porous membrane (Celgard 2320, thickness = 20  $\mu\text{m}$ ) consisting of a PP outer layer and a polyethylene (PE) inner layer. The substrate for the spray application was a film cut into 20 mm squares and fixed on glass. Depositions were performed by varying the substrate temperature from room temperature to 100  $^{\circ}\text{C}$ , the supply amount from 0.5 to 4 mL, and the supply rate from 10 to 60 mL/h, while making  $\text{N}_2$  gas flow in atmospheric pressure.

The surface morphology of each sample was observed before and after spraying using a confocal laser scanning microscope (CLSM, VK-X100, KEYENCE, Higashi Yodogawa, Japan). The inside of the film was observed using a transmission electron microscope (TEM, JEM-2010 MX, JEOL, Akishima, Japan) after cutting and slicing the sample using an ultra-microtome (MT-7000N, Asaka, Japan) after solidifying with resin. TEM samples were prepared for observation in two directions, parallel and perpendicular to the surface of the film. A scanning transmittance electron microscope (STEM, JEM-2010 MX, JEOL, Akishima, Japan) and an energy-dispersive X-ray spectroscope (EDX, JED-2300T, JEOL, Akishima, Japan) were used for elemental analysis of the deposited layer. The effect of spray application on the ionic conductivity determined by the ions passing through the film was investigated using electrochemical impedance spectroscopy (EIS). The measurements were conducted for the sample sandwiched between electrodes with a diameter of 10 mm using a potentiostat (SP-200, Bioscientific Instrument, Vaucanson, France) within the frequency range 0.1–7 MHz at an amplitude of 10 mV. An electrolyte solution contained 1 M of  $\text{LiClO}_4$  in equal volumes of propylene carbonate and diethyl carbonate. EIS is a powerful technique for the characterization of electrochemical systems [40,41]. The films were annealed at 70, 90, 110, 130, and 150  $^{\circ}\text{C}$  for 60 min to investigate the effect of spray application on thermal stability. The film was sandwiched between glasses with a load of 150 g to prevent warping. Structural changes in the film due to annealing were characterized via X-ray diffraction (XRD, MiniFlex600-C HR, Rigaku, Akishima, Japan) using  $\text{CuK}\alpha$  radiation.

### 3. Results and Discussion

#### 3.1. Spray Condition and Deposition State

The evolution of aerosol droplets approaching the hot substrate is shown schematically for cases of different initial droplet sizes. At low temperatures or with a large initial droplet size, the solvent within the droplet was not completely vaporized and the liquid droplet vaporized upon contact with the substrate, leaving a ring-shaped dry precipitate on the substrate. At intermediate temperatures or with a medium droplet size, the solvent was vaporized, and a dry precipitate (an amorphous precursor salt) hit the substrate surface where a pyrolysis reaction took place. At high temperature or with a small droplet size, the vaporized precipitates underwent a chemical reaction in the vapor phase before they reached the substrate surface [15]. In this experiment, large initial droplets and low temperature were used, and the liquid droplets that reached the surface of the membrane penetrated into the pores.

When the MAO/NMP solution was sprayed onto the porous membranes, the formation of deposit layers on the surface and inside was sensitively dependent on the application conditions. We previously reported that the inner deposited layer contributes to improving the thermal stability of a film [24]. On the other hand, surface deposits block the pores and are brittle and flaky in nature. We investigated the relationship between the spray conditions and the deposition state.

##### 3.1.1. Surface Deposition

Typical CLSM images of film surfaces sprayed under various conditions are shown in Figure 1. For the film sprayed under the reference conditions shown in Figure 1a, traces of

small droplets were visible, but there were no large deposit areas and most of the membrane surface was exposed. On the other hand, when the spray application was performed at low substrate temperature (25 °C), the entire surface was covered with deposits, as shown in (b). As the substrate temperature increased, a higher density of small droplet traces was observed. High feeding speed (30 mL/h) resulted in the formation of large lumpy deposits on the surface, as shown in (c). From the viewpoint of process time, 10 mL/h was suitable. As the spray amount increased, rounded deposits appeared and covered the entire surface, as shown in (d). We selected 1 mL as the spray amount because smaller amounts were ineffective.

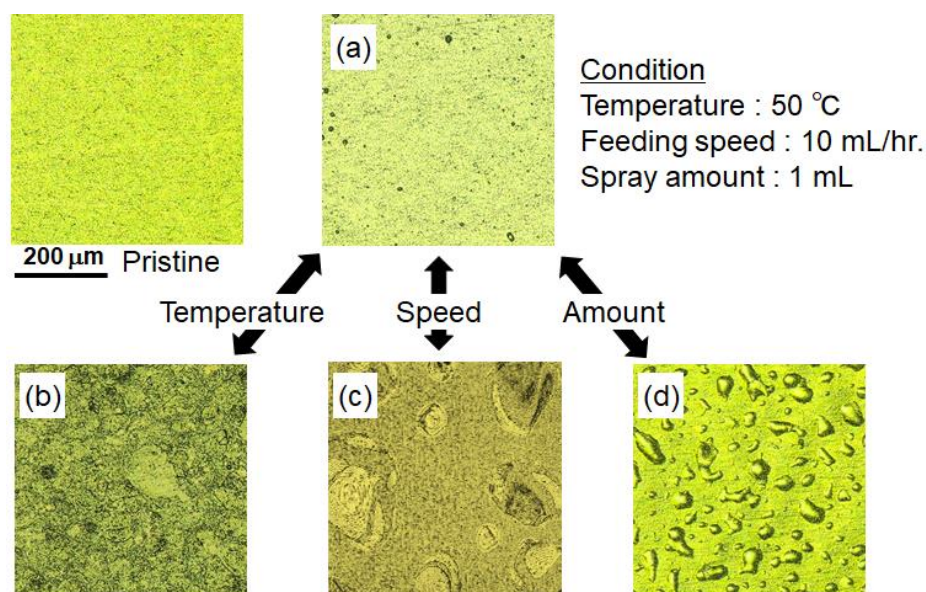


**Figure 1.** Typical CLSM images of film surfaces obtained after spraying under various conditions. (a) Reference condition, (b) substrate temperature: 25 °C, (c) feeding speed: 30 mL/h, (d) spray amount: 4 mL.

### 3.1.2. Internal Deposition

Figure 2 shows XTEM images and the elemental mapping obtained with EDX analysis near the surface of the samples shown in Figure 1a,b. The locations of the XTEM image and elemental mapping were different. In the sample sprayed at a substrate temperature of 50 °C, no layer was deposited on the surface and a black contrast can be observed inside in the XTEM image. Al and O were detected inside the film in the elemental mapping as shown in (a). The black contrast seen in XTEM was formed by Al and O, meaning that the solution penetrated inside. On the other hand, in the sample coated at room temperature (25 °C), a deposited layer was formed on the surface, but Al and O did not penetrate the interior, as seen in (b). The deposited layer peeled off from the surface, as shown in the elemental mapping.

These results were determined by the balance between the penetration of the MAO solution into the membrane, retention on the surface, and solvent (NMP) evaporation. The decrease in temperature slowed down penetration into the interior, and the solution remained on the surface and thick deposits were formed, as shown in Figures 1b and 2b. The droplet size increased with an increase in the feeding speed, and the solution coalesced at the surface and penetrated the interior simultaneously. Then, lumpy deposits were formed, as seen in Figure 1c. When the amount of spray was large, the pores were blocked by the solution, causing the solution to accumulate on the surface due to penetration being prevented, and resulting in the formation of rounded deposits, as seen in Figure 1d. In all cases, the surface deposits showed poor adhesion to the membrane and were not suitable for coating. After comprehensive consideration, we decided on the conditions shown in Figure 1 as the reference process.

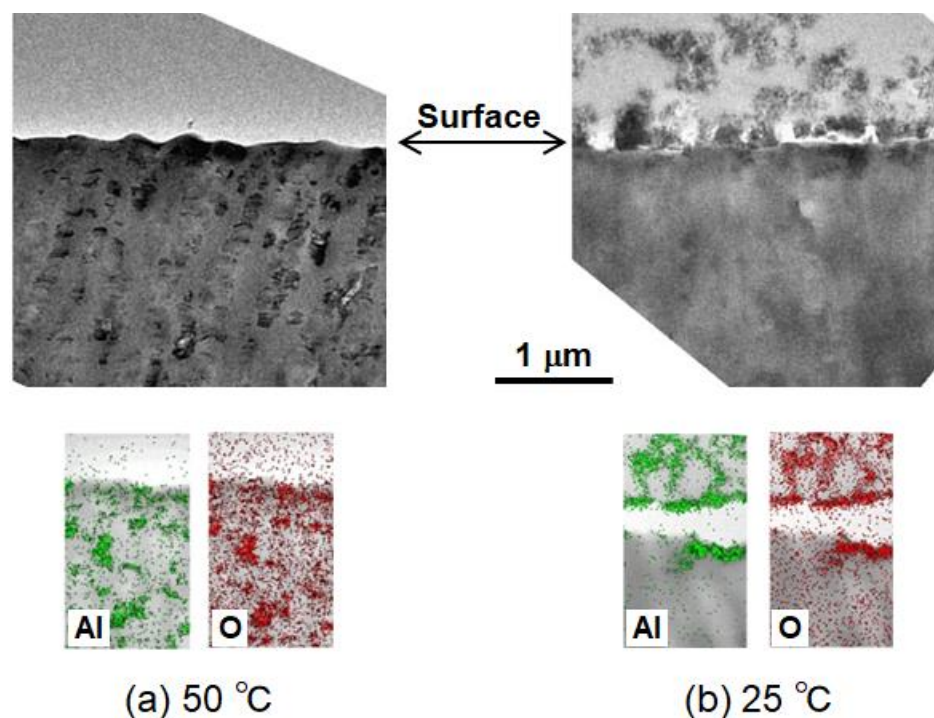


**Figure 2.** XTEM images and the elemental mapping obtained by EDX analysis near surface of films sprayed at each temperature. (a) Film sprayed in reference condition; (b) film sprayed at 25 °C.

### 3.2. Characterization of Deposited Layer

The TEM image of the layer deposited on the surface deformed and became blurred during observation. It can be considered a transition layer before a stable substance was achieved. On the other hand, the image of the internal deposited layer did not change even when observed at high magnification. Therefore, we investigated the internal deposited layer in detail.

#### 3.2.1. Elemental Analysis

Figure 3 shows a STEM image and the elemental mapping obtained by EDX analysis for the plane parallel to the surface of the sample corresponding to Figure 1a. Many black contrasts can be seen in the STEM image (a). These contrasts reflect the absorption of the electron beam by Al and O shown in the distribution maps (b) and (c).

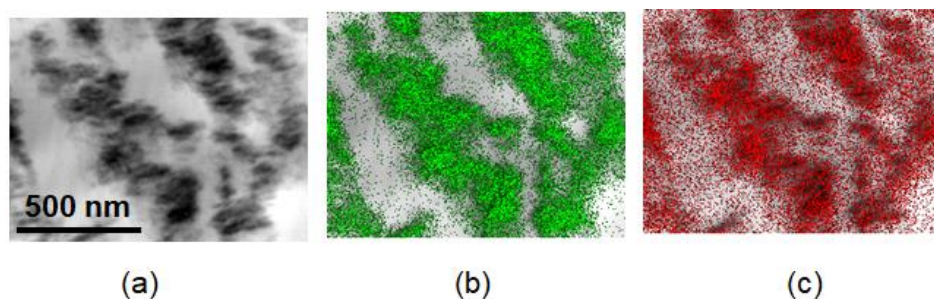


**Figure 3.** STEM/EDX analysis of plane parallel to surface inside sample; (a) STEM image, and elemental mapping of (b) Al atoms and (c) O atoms.

The atomic fractions obtained by the STEM/EDX analysis in Figure 3 are shown in Table 1 by comparing the as-received films. Most of the detected elements were C, as it was the main material of the membrane, but Al and O were detected, with atomic fractions of 3.1% and 5.1%, respectively. The atomic ratio of Al atoms to O atoms calculated from

this result was 0.38 to 0.62. A small amount of O was detected even in the as-received film. These results show that the composition ratio was almost equal to that of  $\text{Al}_2\text{O}_3$ .

**Table 1.** Atomic fraction (%) obtained using STEM/EDX analysis for the films after spray application and as received.

Element	After Spray	As Received
C	91.8	98.8
Al	3.1	0.0
O	5.1	1.2

### 3.2.2. High-Magnification TEM Image

A high-magnification TEM image for the black contrast area shown in Figure 3a and a crystal structure model of  $\text{Al}_2\text{O}_3$  created with a 3D visualization system (VESTA) [42] are shown in Figure 4. The arrangement of Al atoms and O atoms for  $\text{Al}_2\text{O}_3$  is projected along the [1210] axis.  $\text{Al}_2\text{O}_3$  has a hexagonal closed-pack structure, and the lattice constants are  $a$ : 4.7606 Å and  $c$ : 12.994 Å [43]. The interplanar spacing estimated from the lattice image is 2.1 Å and 2.2 Å, which is close to the Al atom arrangement of the crystal structure model. The lattice image suggests that the deposited layer inside the film is  $\text{Al}_2\text{O}_3$ .

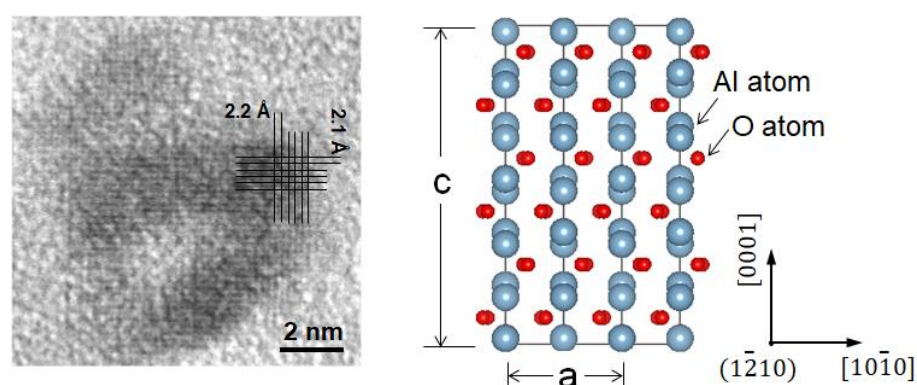


**Figure 4.** Lattice image taken by high-magnification TEM observation and a crystal structure model of  $\text{Al}_2\text{O}_3$  created by VESTA.

The ratio of Al atoms to O atoms obtained by STEM/EDX analysis was almost identical to the composition ratio of  $\text{Al}_2\text{O}_3$ . It is suggested that the interplanar spacing of the lattice image is the atomic arrangement of the  $\text{Al}_2\text{O}_3$  crystal.  $\text{Al}_2\text{O}_3$  films deposited on various substrates using the spray synthesis method have previously been reported [18–21]. However, the process was conducted at a substrate temperature over 300 °C in every report. In contrast, this experiment suggests that the formation of the  $\text{Al}_2\text{O}_3$  layer occurs at substrate temperatures below 100 °C. The formation of  $\text{Al}_2\text{O}_3$  shells using the layer-by-layer MAO coating process has also been reported [44]. An  $\text{Al}_2\text{O}_3$  layer may be formed on the sidewalls of the pores due to the penetration of the solution from spray application. The reaction mechanism of MAO is complex [45]. Further investigation into the formation of  $\text{Al}_2\text{O}_3$  from MAO is required.

### 3.3. Spray Application on Three-Layer Membrane

We applied an MAO/NMP solution to a three-layer membrane using the reference conditions shown in the previous chapter. The membrane consisted of two outer PP layers and an inner PE layer. The PP-based layer provides high-temperature melt integrity and oxidation resistance, and the PE-based layer provides high-speed shutdown features. The PP layer has uniaxial residual strain caused by the dry technique used to produce porous membranes, and the PE layer prepared using the wet technique is uniform, or has biaxial residual strain caused by the manufacturing process [46]. This film is stretched in one

direction during the manufacturing process, thereby possessing a residual strain along the machine direction (MD).

The inside of the sprayed membrane was analyzed using XTEM and STEM/EDX. In order to check the effectiveness of spraying, we investigated resistance measurements using EIS and thermal stability through heating experiments.

### 3.3.1. Internal Observation

The XTEM images and the EDX analysis obtained using STEM after cutting and slicing the sprayed film in the depth direction are shown in Figure 5. The PP layers on both sides and the PE layer in the middle can be observed in the upper overall image. A lot of black contrast can be seen from the surface to a depth of several microns on the sprayed side, and it is hardly visible on the back side. The black contrast reflects the absorption of the electron beam by Al and O shown in the lower distribution maps. Al and O are present in the black contrast area on the spray side, but they are almost at noise level in the middle and back side. As described in the previous chapter, a deposited layer of  $\text{Al}_2\text{O}_3$  was formed inside the spray side.

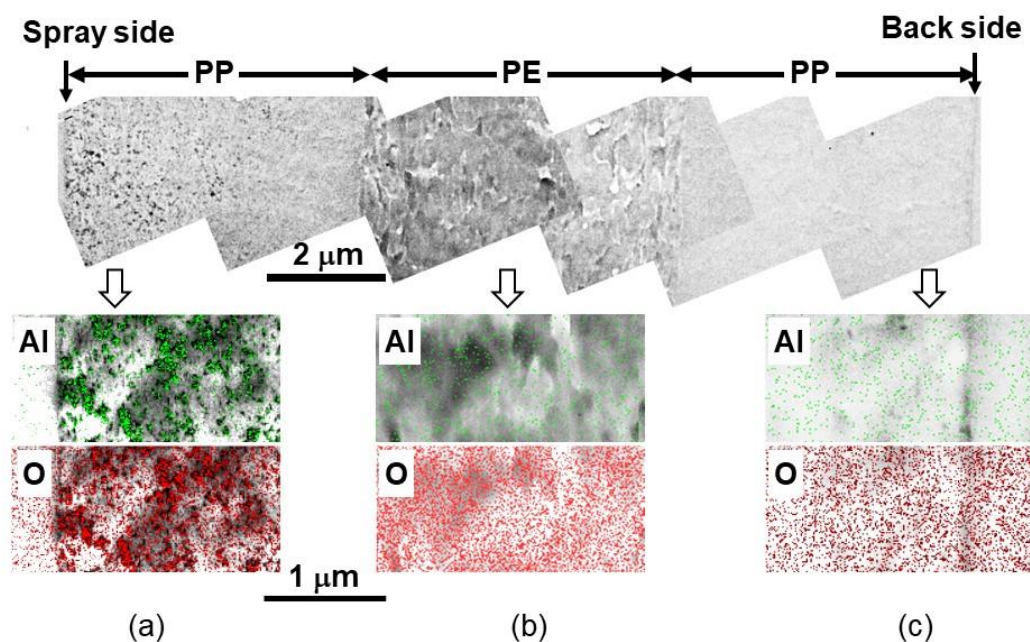
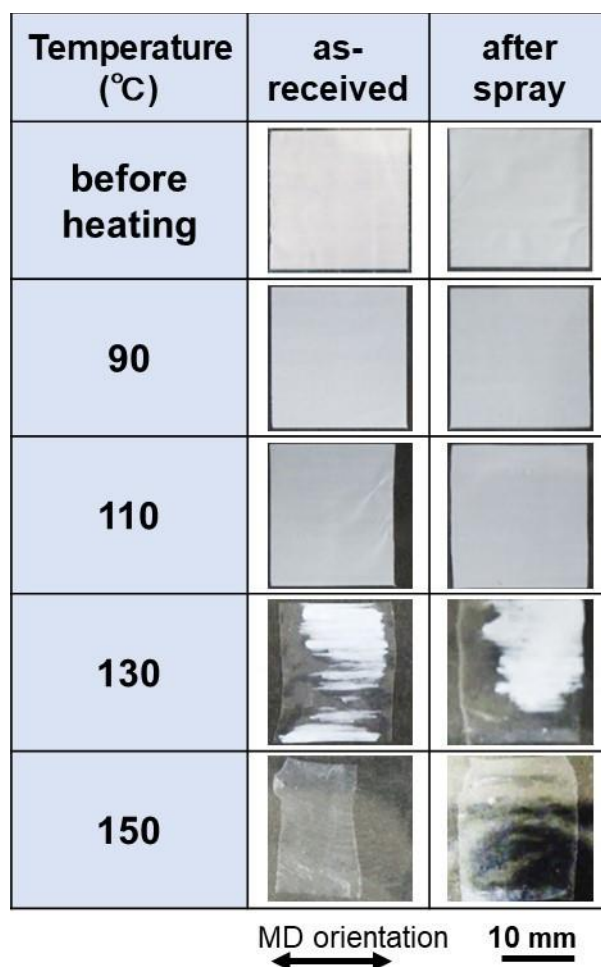


**Figure 5.** XTEM observation and the elemental mapping obtained by STEM/EDX for the sprayed film. Upper: overall image of film cross-section; lower: elemental mapping of Al atoms and O atoms (a) near sprayed surface, (b) at mid portion, and (c) near back side.

### 3.3.2. Effect of Spray Application on Thermal Stability

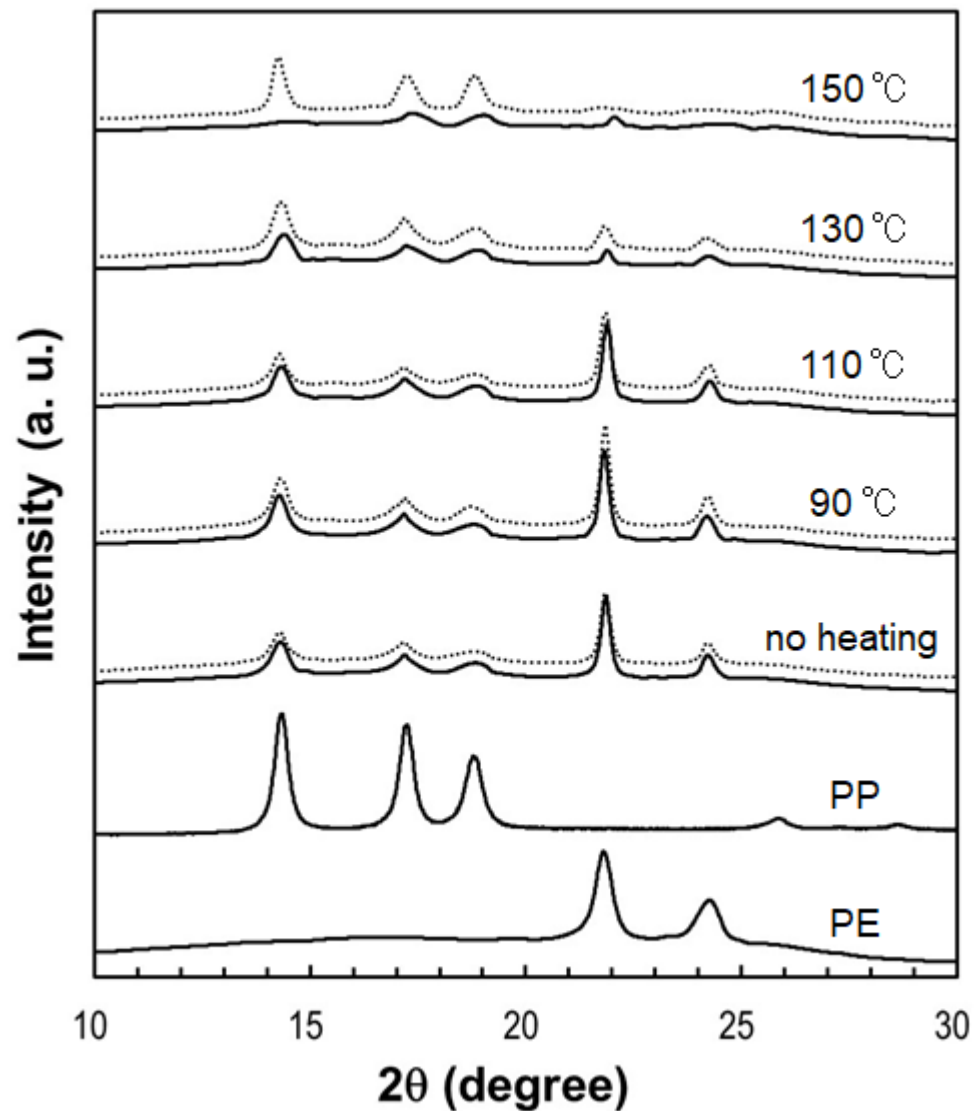
The working temperature is normally 90 °C or less, but we investigated a thermal stability up to 150 °C assuming a case of abnormal conditions. Figure 6 shows photographs of the film after annealing at each temperature for 60 min, comparing the as-received film and after spraying. There were no changes in both films at temperatures below 90 °C. The films shrank along the MD orientation at temperatures above 110 °C and did not shrink vertically. This means that the shrinkage was caused by the residual strain above the temperature at which the film softens. The thermal behavior of pristine PE separators varies greatly depending on the report, with some cases showing significant shrinkage and some cases showing almost no shrinkage [36,37]. This suggests that the thermal shrinkage of the separator is greatly influenced by the manufacturing process. The residual strain of this separator was a major factor in thermal shrinkage. The shrinkage rate was suppressed after spraying compared to the as-received film. At temperatures above 130 °C, the melted

part of the film became transparent, and the shrinkage rate increased significantly. The films entirely melted at 150 °C.



**Figure 6.** Photographs of film after heating for 60 min at each temperature. A comparison is made between as-received film and after spray application. As the heating temperature increased, the shrinkage and melt of the film progressed. Spray application slightly suppressed the shrinkage of film.

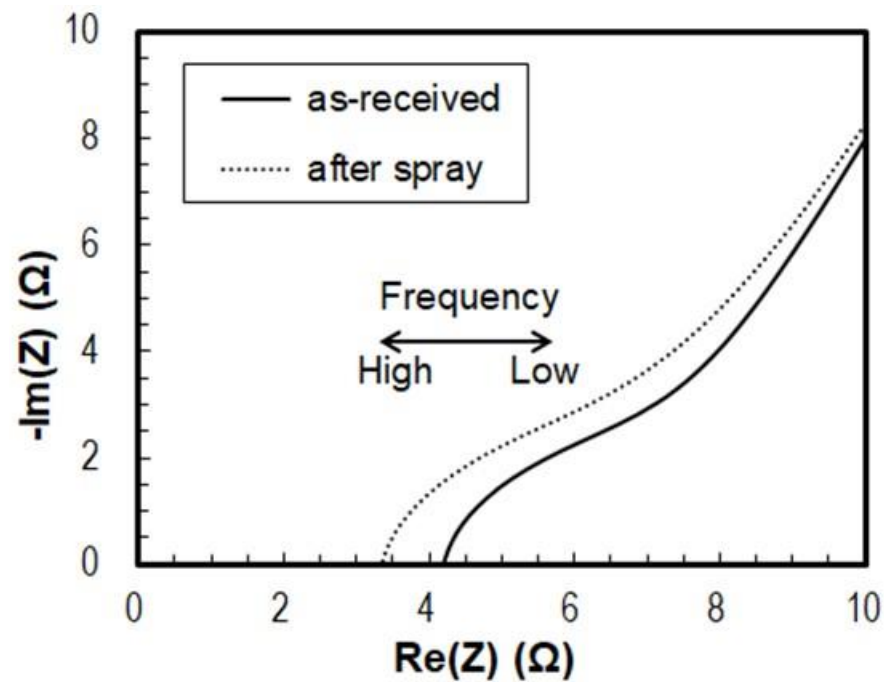
The XRD spectra of separators after annealing at each temperature for 60 min, comparing the sample as-received (solid line) and after spraying (dotted line), are shown in Figure 7. The PP layer fabricated by the dry process and the PE layer fabricated by the wet process are also shown for comparison. In the three-layer separator used in this study, peaks due to the PP layer and PE layer were observed. A peak due to  $Al_2O_3$  was not observed, because the amount of internal deposition was too small. There was no significant change in peak intensity at temperatures below 110 °C for both films before and after spraying. At temperatures above 130 °C, the peak intensity of the PE layer decreased for both films with and without spraying. At 150 °C, the peaks of both the PP and the PE layers almost disappeared in the as-received film. This decrease in the peaks of each layer after annealing indicates that each layer changed from crystalline to amorphous due to the melting of the film seen in Figure 6. In contrast, the peaks of the PP layer remained in the sprayed film. This indicates that the spray application suppressed the melting of the PP layer.



**Figure 7.** XRD spectrum after annealing at each temperature for samples as-received (—) and after spraying (· · · · ·). Peaks due to the PP layer and PE layer are observed. At 150 °C, the peaks of both the PP and PE layers almost disappear in the film before spraying, while the peaks of the PP layer remain after spraying.

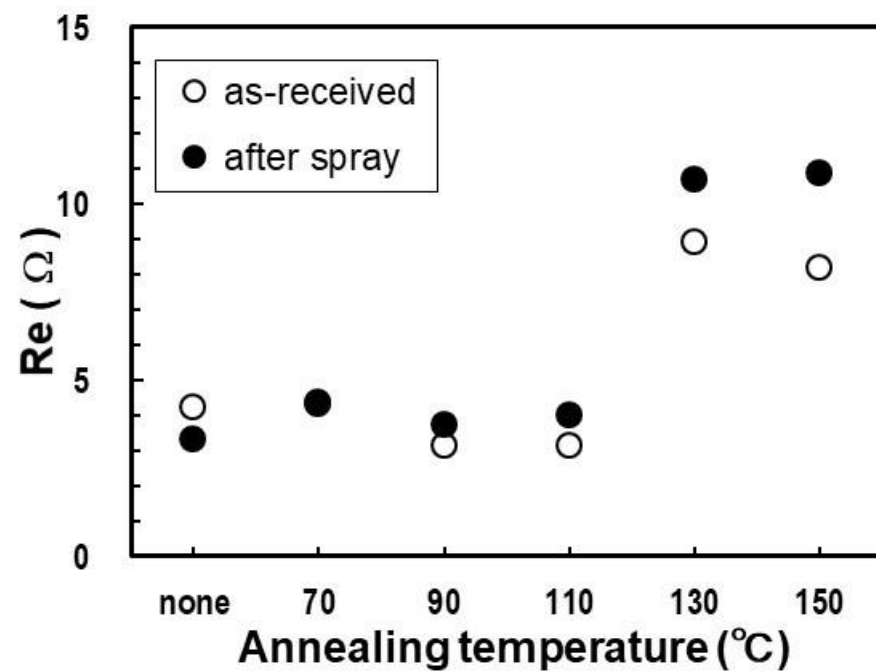
### 3.3.3. Effect of Spray Application on Resistance

Figure 8 shows the Nyquist plots obtained with EIS, comparing samples before and after spraying as examples. The negative imaginary impedance ( $-\text{Im}(Z)$ ) is plotted versus the real part of the impedance ( $\text{Re}(Z)$ ). In a real electrochemical system, the pattern of a Nyquist plot usually shows a semicircle in high-frequency areas and straight lines in low-frequency areas, corresponding to the electrochemical processes controlled by charge and mass transfer, respectively [47]. In this system, the resistance determined by the  $\text{Li}^+$  ion conductivity of the separator is obtained from the intersection of the curve and the horizontal axis.



**Figure 8.** Nyquist plots obtained with EIS for samples as-received and after spraying.

Figure 9 shows the relationship between the resistance of the separator obtained from the Nyquist plot and annealing temperature. At temperatures below 110 °C, there is no change in resistance, and no difference before and after spraying. The resistance increases significantly at temperatures above 130 °C and the melting of films occurs, as seen in Figure 6. This means that the pores in the separator are closed by melting and the movement of ions is suppressed, i.e., shutdown occurs.



**Figure 9.** Resistance determined from the intersection of the curve and the horizontal axis after annealing for 60 min at each temperature for samples as-received and after spraying. The resistance increases significantly at temperatures above 130 °C due to melting of the PE layer.

### 3.3.4. Model of Improved Thermal Stability

Figure 10 shows the effect of the spray application of an MAO/NMP solution on thermal stability. In this study, a separator with a three-layer PP/PE/PP structure was used. The melting points were 165 °C for PP and 115–135 °C for PE. The shape of the separator was maintained until 90 °C but began to shrink due to residual strain with rising temperature, as shown in Figure 6. At 130 °C near the melting point of PE, the PE layer began to melt, as shown by the decrease in the XRD peaks. The PP layer melted at 150 °C, making the entire film transparent and reducing the XRD peaks.

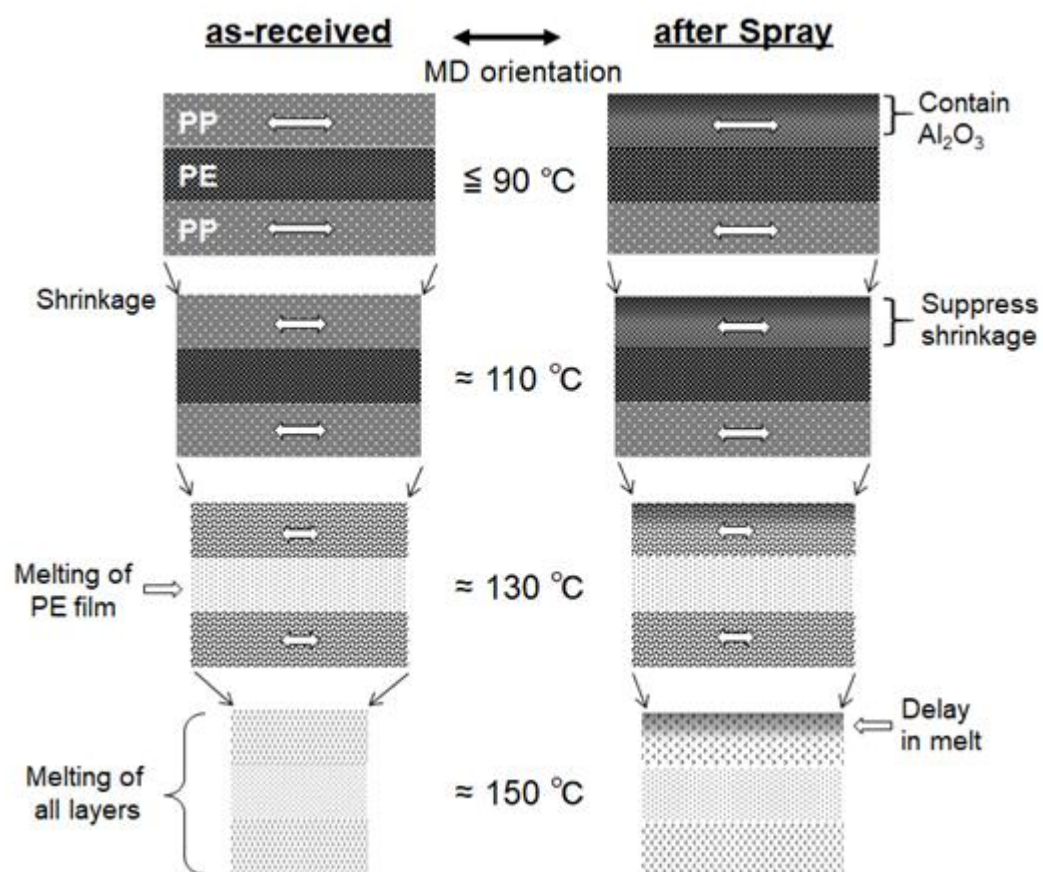


**Figure 10.** Schematic images of three-layer separator shrinkage due to annealing.  $\text{Al}_2\text{O}_3$  formed inside the film suppresses shrinkage and delays dissolution at high temperatures.

In contrast, a deposited layer was formed on the pore-sidewall of the PP layer on the spray side for the sprayed film, as seen in Figure 5. This deposit layer contributed to improved strength, and the shrinkage rate reduced compared to the as-received separator at temperatures over 110 °C. Particularly at 150 °C, the difference between the XRD peaks of both films became significant, as seen in Figure 7. The peaks due to the PP layer were greatly reduced for the as-received film, whereas they were hardly reduced for the sprayed film. This suggests that the deposited layer slows down the progress of melting for the PP layer, resulting in suppressed shrinkage.

## 4. Conclusions

Depositions were conducted on a monolayer porous membrane using the spray synthesis method, varying conditions such as the substrate temperature, feeding speed, and spray amount using an MAO/NMP solution. Ultra-thin layers were formed by the penetrated solution on the wall of the pores inside the membrane. The lattice image and atomic fraction suggested that this thin layer was  $\text{Al}_2\text{O}_3$ . The formation of  $\text{Al}_2\text{O}_3$  occurred at lower temperatures than in previous reports. A reaction like the layer-by-layer method

may occur while the solution is penetrating inside the membrane. The mechanism of Al<sub>2</sub>O<sub>3</sub> formation from an MAO solution requires further investigation. The spray condition was determined based on the finding that there was no deposited layer on the surface, and thin layers were formed inside the membrane. It was confirmed that shrinkage and melting at high temperatures can be suppressed for a three-layer separator sprayed in the conditions through heating experiments and XRD analysis. The Al<sub>2</sub>O<sub>3</sub> layer inside the membrane contributes to improving the thermal stability of the film. The resistance of the separator did not increase with spraying, indicating that the inner Al<sub>2</sub>O<sub>3</sub> layer did not block pores and did not affect ion conduction. This process can be expected to find wider applications in low-melting-point materials such as polyolefin.

**Author Contributions:** Conceptualization, M.I., T.K., A.M. and K.Y.; methodology, M.I., T.K. and K.Y.; validation, M.I., T.K., A.M. and K.Y.; formal analysis, M.I.; investigation, M.I., T.K., A.M., M.A., H.M. and Y.K.; resources, M.A. and H.M.; data curation, M.I. and K.Y.; writing—original draft preparation, M.I.; writing—review and editing, M.I. and K.Y.; supervision, K.Y.; project administration, K.Y.; funding acquisition, A.M. All authors have read and agreed to the published version of the manuscript.

**Funding:** This research received no external funding.

**Data Availability Statement:** The data presented in this study are available on request from the corresponding author. The data are not publicly available, due to privacy.

**Acknowledgments:** We are grateful to T. Haraguchi for the kind assistance in the characterization of TEM observation and STEM/EDX analysis and K. Hisatomi for the assistance in experiments at the University of Miyazaki.

**Conflicts of Interest:** Atsushi Miyazawa was employed by the Tosoh Corporation, and Masahiro Aoki and Haruna Mori were employed by the Tosoh Finechem Corporation. Tadahiko Kubota, president of the Yokohama Battery Science Corporation, participated in this study as a researcher. All authors declare that the research was conducted in the absence of any commercial or financial relationships that could be construed as a potential conflict of interest.

## References

1. Haleem, A.M.A.; Ichimura, M. Electrochemical deposition of aluminum oxide thin films from aqueous baths. *Mater. Lett.* **2014**, *130*, 26–28. [[CrossRef](#)]
2. Lale, A.; Scheid, E.; Cristiano, F.; Datas, L.; Reig, B.; Launay, J.; Temple-Boyer, P. Study of aluminium oxide thin films deposited by plasma-enhanced atomic layer deposition from tri-methyl-aluminium and dioxygen precursors: Investigation of interfacial and structural properties. *Thin Solid Films* **2018**, *666*, 20–27. [[CrossRef](#)]
3. Pugliese, A.; Shyam, B.; Repa, G.M.; Nguyen, A.H.; Mehta, A.; Webb, E.B., III; Fredin, L.A.; Strandwitz, N.C. Atomic-Layer-Deposited Aluminum Oxide Thin Films Probed with X-ray Scattering and Compared to Molecular Dynamics and Density Functional Theory Models. *ACS Omega* **2022**, *7*, 41033–41043. [[CrossRef](#)] [[PubMed](#)]
4. Yang, Y.; Huang, X.; Cao, Z.; Chen, G. Thermally conductive separator with hierarchical nano/microstructures for improving thermal management of batteries. *Nano Energy* **2016**, *22*, 301–309. [[CrossRef](#)]
5. Liang, X.; Yang, Y.; Jin, X.; Huang, Z.; Kang, F. The high performances of SiO<sub>2</sub>/Al<sub>2</sub>O<sub>3</sub>-coated electrospun polyimide fibrous separator for lithium-ion battery. *J. Membr. Sci.* **2015**, *493*, 1–7. [[CrossRef](#)]
6. Qi, S.; Porotnikova, N.M.; Ananyev, M.V.; Kuzmin, A.V.; Eremin, V.A.; Pankratov, A.A.; Molchanova, N.G.; Reznitskikh, O.G.; Farlenkov, A.S.; Vovkotrub, E.G.; et al. High-temperature glassy-ceramic sealants SiO<sub>2</sub>—Al<sub>2</sub>O<sub>3</sub>—BaO—MgO and SiO<sub>2</sub>—Al<sub>2</sub>O<sub>3</sub>—ZrO<sub>2</sub>—CaO—Na<sub>2</sub>O for solid oxide electrochemical devices. *Trans. Nonferrous Met. Soc. China* **2016**, *26*, 2916–2924. [[CrossRef](#)]
7. Ananchenko, D.V.; Nikiforov, S.V.; Kuzovkov, V.N.; Popov, A.I.; Ramazanov, G.R.; Batalov, R.I.; Bayazitov, R.M.; Novikov, H.A. Radiation-induced defects in sapphire single crystals irradiated by a pulsed ion beam, Radiation-induced defects in sapphire single crystals irradiated by a pulsed ion beam. *Nucl. Instruments Methods Phys. Res. Sect. B* **2020**, *466*, 1–7. [[CrossRef](#)]
8. Kumar, N.A.P.K.; Leonard, K.J.; Jellison, G.E.; Snead, L.L. High-Dose Neutron Irradiation Performance of Dielectric Mirrors. *Fusion Sci. Technol.* **2015**, *67*, 771–783. [[CrossRef](#)]
9. Lin, S.-C.; Wang, C.-C.; Tien, C.-L.; Tung, F.-C.; Wang, H.-F.; Lail, S.-H. Fabrication of Aluminum Oxide Thin-Film Devices Based on Atomic Layer Deposition and Pulsed Discrete Feed Method. *Micromachines* **2023**, *14*, 279. [[CrossRef](#)]
10. Rabha, M.B.; Salem, M.; El Khakani, M.A.; Bessais, B.; Gaidi, M. Monocrystalline silicon surface passivation by Al<sub>2</sub>O<sub>3</sub>/porous silica combined treatment. *Mater. Sci. Eng. B* **2013**, *178*, 695–697. [[CrossRef](#)]
11. Zhou, G.; Wang, L.; Wang, X.; Yub, Y.; Mutzke, A. Effect of bias voltage on microstructure and optical properties of Al<sub>2</sub>O<sub>3</sub> thin films prepared by twin targets reactive high power impulse magnetron sputtering. *Vacuum* **2019**, *166*, 88–96. [[CrossRef](#)]

12. Jo, J.-W.; Kim, K.-H.; Kim, J.; Ban, S.G.; Kim, Y.-H.; Park, S.K. High-Mobility and Hysteresis-Free Flexible Oxide Thin-Film Transistors and Circuits by Using Bilayer Sol–Gel Gate Dielectrics. *ACS Appl. Mater. Interfaces* **2018**, *10*, 2679–2687. [[CrossRef](#)]
13. Dhonge, B.P.; Mathews, T.; Sundari, S.T.; Thinaharan, C.; Kamruddin, M.; Dash, S.; Tyagi, A.K. Spray pyrolytic deposition of transparent aluminum oxide (Al<sub>2</sub>O<sub>3</sub>) films. *Appl. Surf. Sci.* **2011**, *258*, 1091–1096. [[CrossRef](#)]
14. Aguilar-Frutis, M.; Garcia, M.; Falcony, C. Optical and electrical properties of aluminum oxide films deposited by spray pyrolysis. *Appl. Phys. Lett.* **1998**, *72*, 1700–1702. [[CrossRef](#)]
15. Falcony, C.; Aguilar-Frutis, M.A.; García-Hipólito, M. Spray Pyrolysis Technique; High-K Dielectric Films and Luminescent Materials: A Review. *Micromachines* **2018**, *9*, 414. [[CrossRef](#)]
16. Workie, A.B.; Ningsih, H.S.; Shih, S.-J. A comprehensive review on the spray pyrolysis technique: Historical context, operational factors, classifications, and product applications. *J. Anal. Appl. Pyrolysis* **2023**, *170*, 105915. [[CrossRef](#)]
17. Avvaru, B.; Patil, M.N.; Gogate, P.R.; Pandit, A.B. Ultrasonic atomization: Effect of liquid phase properties. *Ultrasonics* **2006**, *44*, 146–158. [[CrossRef](#)] [[PubMed](#)]
18. Khatibani, A.B.; Rozati, S.M. Optical and morphological investigation of aluminium and nickel oxide composite films deposited by spray pyrolysis method as a basis of solar thermal absorber. *Bull. Mater. Sci.* **2015**, *38*, 319–326. [[CrossRef](#)]
19. Patil, P.S. Versatility of chemical spray pyrolysis technique. *Mater. Chem. Phys.* **1999**, *59*, 185–198. [[CrossRef](#)]
20. Kate, R.S.; Pathan, H.M.; Kalubarme, R.; Kale, B.B.; Deokate, R.J. Spray pyrolysis: Approaches for nanostructured metal oxide films in energy storage application. *J. Energy Storage* **2022**, *54*, 105387. [[CrossRef](#)]
21. Maho, A.; Nayak, S.; Gillissen, F.; Cloots, R.; Rougier, A. Film Deposition of Electrochromic Metal Oxides through Spray Coating: A Descriptive Review. *Coatings* **2023**, *13*, 1879. [[CrossRef](#)]
22. Yoshino, K.; Takemoto, Y.; Oshima, M.; Toyota, K.; Inaba, K.; Haga, K.; Tokudome, K. Low-Temperature Growth of ZnO Films by Spray Pyrolysis. *Jpn. J. Appl. Phys.* **2011**, *50*, 040207. [[CrossRef](#)]
23. Imai, M.; Watanabe, M.; Mochihara, A.; Tominaga, H.; Yoshino, K.; Shen, Q.; Toyoda, T.; Hayase, S. Atmospheric growth of ZnO films deposited by spray pyrolysis using diethylzinc solution. *J. Cryst. Growth* **2017**, *468*, 473–476. [[CrossRef](#)]
24. Imai, M.; Kubota, T.; Miyazawa, A.; Aoki, M.; Mori, H.; Komaki, Y.; Yoshino, K. Ultra-Thin Layer Inside Separator Deposited by Spray Pyrolysis Using Methylaluminoxane Solution. *Cryst. Res. Technol.* **2022**, *58*, 2200203. [[CrossRef](#)]
25. McAllister, J.A.; Farrell, A.E. Electricity consumption by battery-powered consumer electronics: A household-level survey. *Energy* **2007**, *32*, 1177–1184. [[CrossRef](#)]
26. Agrawal, R.; Pandey, G. Solid polymer electrolytes: Materials designing and all-solid-state battery applications: An overview. *J. Phys. D Appl. Phys.* **2008**, *41*, 223001. [[CrossRef](#)]
27. Fu, D.; Luan, B.; Argue, S.; Bureau, M.N.; Davidson, I.J. Nano SiO<sub>2</sub> particle formation and deposition on polypropylene separators for lithium-ion batteries. *J. Power Sources* **2012**, *206*, 325–333. [[CrossRef](#)]
28. Placke, T.; Kloepsch, R.; Dühnen, S.; Winter, M. Lithium ion, lithium metal, and alternative rechargeable battery technologies: The odyssey for high energy density. *J. Solid State Electrochem.* **2017**, *21*, 1939–1964. [[CrossRef](#)]
29. Dunn, B.; Kamath, H.; Tarascon, J.-M. Electrical energy storage for the grid: A battery of choices. *Science* **2011**, *334*, 928–935. [[CrossRef](#)] [[PubMed](#)]
30. Goodenough, J.B.; Kim, Y. The Li-Ion Rechargeable Battery: A Perspective. *J. Am. Chem. Soc.* **2013**, *135*, 1167–1176. [[CrossRef](#)] [[PubMed](#)]
31. Lagadec, M.F.; Zahn, R.; Wood, V. Characterization and performance evaluation of lithium-ion battery separators. *Nat. Energy* **2019**, *4*, 16–25. [[CrossRef](#)]
32. Ali, S.; Tan, C.; Waqas, M.; Lv, W.; Wei, Z.; Wu, S.; Al-Bogami, A.S.; Lu, J.; Amine, K. Highly Efficient PVDF-HFP/Colloidal Alumina Composite Separator for High-Temperature Lithium-Ion Batteries. *Adv. Mater. Interfaces* **2018**, *5*, 1701147. [[CrossRef](#)]
33. Luiso, S.; Fedkiw, P. Lithium-ion battery separators: Recent developments and state of art. *Curr. Opin. Electrochem.* **2020**, *20*, 99–107. [[CrossRef](#)]
34. Jeong, H.-S.; Kim, D.-W.; Jeong, Y.U.; Lee, S.-Y. Effect of phase inversion on microporous structure development of Al<sub>2</sub>O<sub>3</sub>/poly(vinylidene fluoride-hexafluoropropylene)-based ceramic composite separators for lithium-ion batteries. *J. Power Sources* **2010**, *195*, 6116–6121. [[CrossRef](#)]
35. Choi, J.-A.; Kim, S.H.; Kim, D.-W. Enhancement of thermal stability and cycling performance in lithium-ion cells through the use of ceramic-coated separators. *J. Power Sources* **2010**, *195*, 6192–6196. [[CrossRef](#)]
36. Cai, H.; Yang, G.; Meng, Z.; Yin, X.; Zhang, H.; Tang, H. Water-Dispersed Poly(p-Phenylene Terephthamide) Boosting Nano-Al<sub>2</sub>O<sub>3</sub>-Coated Polyethylene Separator with Enhanced Thermal Stability and Ion Diffusion for Lithium-Ion Batteries. *Polymers* **2019**, *11*, 1362. [[CrossRef](#)] [[PubMed](#)]
37. Ahn, J.H.; You, T.-S.; Lee, S.-M.; Esken, D.; Dehe, D.; Huang, Y.-C.; Kim, D.-W. Hybrid separator containing reactive, nanostructured alumina promoting in-situ gel electrolyte formation for lithium-ion batteries with good cycling stability and enhanced safety. *J. Power Sources* **2020**, *472*, 228519. [[CrossRef](#)]
38. Chen, E.Y.-X.; Marks, T.J. Cocatalysts for Metal-Catalyzed Olefin Polymerization: Activators, Activation Processes, and Structure–Activity Relationships. *Chem. Rev.* **2000**, *100*, 1391–1434. [[CrossRef](#)]
39. Wood, D.L.; Li, J.; Daniel, C. Prospects for reducing the processing cost of lithium ion batteries. *J. Power Sources* **2015**, *275*, 234–242. [[CrossRef](#)]

40. Momma, T.; Matsunaga, M.; Mukoyama, D.; Osaka, T. Ac impedance analysis of lithium ion battery under temperature control. *J. Power Sources* **2012**, *216*, 304–307. [[CrossRef](#)]
41. Gunter, F.J.; Habedank, J.B.; Schreiner, D.; Neuwirth, T.; Gilles, R.; Reinhart, G. Introduction to Electrochemical Impedance Spectroscopy as a Measurement Method for the Wetting Degree of Lithium-Ion Cells. *J. Electrochem. Soc.* **2018**, *165*, A3249–A3256. [[CrossRef](#)]
42. Momma, K.; Izumi, F. VESTA 3 for Three-Dimensional Visualization of Crystal, Volumetric and Morphology Data. *J. Appl. Crystallogr.* **2011**, *44*, 1272. [[CrossRef](#)]
43. Tsirelson, V.; Antipin, M.; Gerr, R.; Ozerov, R.; Struchkov, Y. Ruby structure peculiarities derived from X-ray diffraction data. Localization of chromium atoms and electron deformation density. *Phys. Status Solidi A* **1985**, *87*, 425–433. [[CrossRef](#)]
44. Li, Z.; Fredin, L.A.; Tewari, P.; DiBenedetto, S.A.; Lanagan, M.T.; Ratner, M.A.; Marks, T.J. In Situ Catalytic Encapsulation of Core-Shell Nanoparticles Having Variable Shell Thickness: Dielectric and Energy Storage Properties of High-Permittivity Metal Oxide Nanocomposites. *Chem. Mater.* **2010**, *22*, 5154–5164. [[CrossRef](#)]
45. Teixeira, V.E.; Livotto, P.R. The mechanism of the reaction between MAO and TMA: DFT study of the electronic structure and characterization of transition states for [AlOMe]<sub>6</sub>, [AlOMe]<sub>9</sub> and [AlOMe]<sub>16</sub> cages. *J. Mol. Graph. Model.* **2020**, *99*, 107626. [[CrossRef](#)]
46. Love, C.T. Thermomechanical analysis and durability of commercial micro-porous polymer Li-ion battery separators. *J. Power Sources* **2011**, *196*, 2905–2912. [[CrossRef](#)]
47. Lazanas, A.C.; Prodromidis, M.I. Electrochemical Impedance Spectroscopy-A Tutorial. *ACS Meas. Sci. Au* **2023**, *3*, 162–169. [[CrossRef](#)]

**Disclaimer/Publisher’s Note:** The statements, opinions and data contained in all publications are solely those of the individual author(s) and contributor(s) and not of MDPI and/or the editor(s). MDPI and/or the editor(s) disclaim responsibility for any injury to people or property resulting from any ideas, methods, instructions or products referred to in the content.